

## MODELING AND SIMULATIONS OF DEFORMATION AND TRANSPORT IN PEM FUEL CELLS

Serhat Yesilyurt

Sabanci University, Istanbul, Turkey

### ABSTRACT

Performance degradation and durability of PEM fuel cells depend strongly upon transport and deformation characteristics of their components especially the polymer membrane. Physical properties of the membrane, such as its ionic conductivity and Young's modulus depend on its water content, which varies significantly with operating conditions and during transients. Recent studies indicate that cyclic transients may induce hygrothermal fatigue that leads to the ultimate failure of the membrane shortening its lifetime, and thus, hindering the reliable use of PEM fuel cells for automotive applications. In this work, we present two-dimensional simulations and analysis of coupled deformation and transport in PEM fuel cells. A two-dimensional cross-section of anode and cathode gas diffusion layers, and the membrane sandwiched between them is modeled using Maxwell-Stefan equations in the gas diffusion layers, Biot's poroelasticity and Darcy's law for deformation and water transport in the membrane and Ohm's law for ionic currents in the membrane and electric currents in the gas diffusion electrodes. Steady-state deformation and transport of water in the membrane, transient responses to step changes in load and relative humidity of the anode and cathode are obtained from simulation experiments, which are conducted by means of a commercial finite-element package, COMSOL Multiphysics.

### INTRODUCTION

Design of PEM fuel cells is a challenging task for automotive applications due to durability and reliability constraints, which are particularly stringent as the incumbent internal-combustion-engine technology, has been perfected for over a century. Failure of PEM fuel cells are mostly due to degradation of materials during transients which include startup, shutdown, electric load demands and control inputs [1]. Fatigue mechanism is among the most suspected ones that lead to catastrophic failure of the components following mild-to-severe performance degradation [1-3].

Major portion of PEM fuel cell modeling efforts concentrate on transport of reactants and water, and its importance on the electrochemical performance of fuel cells, e.g. [4-7]. Transport studies are hard to extrapolate to understand structural aspects that lead to degradation and failure. Moreover, there are several structural modeling and analysis of PEM fuel cells that are not coupled to the transport and electrochemical aspects of PEM fuel cell operation, e.g. [2,8,9].

Modeling of coupled deformation of components and transport of species in PEM fuel cells is recently attracting attention. Choi et al [10] use a thermodynamic model to address swelling of PEM fuel cell membranes, typically Nafion, by means of chemical potential of the water in the membrane where the stretching of polymers affects the osmotic pressure. In their model, Flory-Huggins theory, which relates the volume fraction to the swelling pressure (water pressure in the membrane), and Young's modulus of the membrane are used to address the role of mechanical stresses in the polymer matrix on the sorption of water [10]. Nazarov and Promislow [11] developed a model, which uses the capillary pressure effect only at the boundaries where the membrane is in contact with water vapor, but uses mechanical force balance in the polymer matrix and water pressure in the pores.

In this work, we use Biot's linear poroelasticity to model the elastic deformation of the membrane matrix with the consideration of liquid pressure in pores of the solid matrix. Poroelastic theory uses the force balance between the liquid and the solid phase using linear elasticity [12]. Capillary effects only count at the interface where the liquid phase is exposed to gas similar to the model presented in [11]. The liquid is allowed to move in and out within the matrix using Darcy's Law [13]. Thus, the driving forces of the transport are directly coupled with the mechanical forces of the medium. Furthermore, the model allows the consideration of damping effect due to flow of the liquid in the porous solid during transients.

In the model, which is presented here transport of gas species in gas diffusion layers is modeled by Maxwell-Stefan equa-

tions, advection of the gas mixture in the anode gas diffusion layer is modeled by Darcy's Law subject to conservation of mass, charge transport is modeled by Ohm's Law subject to conservation of charge, and deformation is modeled by plane-strain formulation of the linear elasticity, which included poro-elastic effects only within the membrane, and the water transport in the membrane is modeled by using the Schlogl velocity. Coupled equations are solved using a commercial finite-element code, COMSOL [14].

## DESCRIPTION OF THE MODEL

Two-dimensional model of the PEM fuel cell cross section, which includes gas diffusion layers (GDL) and the membrane is shown in Figure 1. The catalyst layers are assumed relatively thin compared to the membrane, and averaged out in in-plane direction; their effects are considered at the membrane-GDL interfaces. Geometric parameters and values of the two-dimensional section of the membrane are listed in Table 1.

**TABLE 1: GEOMETRIC PROPERTIES OF THE TWO-DIMENSIONAL PEM FUEL CELL SECTION**

Geometric property	Value
Anode and cathode gas flow channel widths, $\ell_{ch}$	1 mm
Anode and cathode shoulder widths, $\ell_{sh}$	1 mm
Anode and cathode gas diffusion layer thicknesses, $\delta_{GDL}$	0.2 mm
Membrane thickness, $\delta_m$	0.05 mm
Anode and cathode catalyst layer thicknesses, $\delta_{CL}$	0.01 mm

## Governing equations

### Transport of gas species in GDLs

Maxwell-Stefan equations are used for modeling the transport of  $H_2$  and  $H_2O$  vapor in the anode GDL and  $O_2$ ,  $H_2O$  vapor and  $N_2$  in the cathode GDL as presented in [6,15]:

$$\frac{\partial}{\partial t}(\rho w_i) + \nabla \left[ -\rho w_i \sum_{j=1}^N D_{ij} \left\{ \left[ \nabla x_j + (x_j - w_j) \frac{\nabla p}{p} \right] \right\} \right] + \rho w_i \mathbf{u} = 0 \quad (1)$$

In (1)  $w$  is mass and  $x$  is molar fraction of the  $i^{th}$  species;  $i$  is  $\{H_2, H_2O\}$  on the anode side, and  $\{O_2, H_2O, N_2\}$  on the cathode side;  $\rho$  is the density of the mixture;  $D_{ij}$  is the binary diffusion coefficient of species  $i$  and  $j$ , which is replaced by the effective diffusion coefficient,  $D_{ij}^{eff} = D_{ij} \epsilon_g^{1.5}$  for porous GDLs having porosity of  $\epsilon_g$ ;  $p$  is pressure, which is assumed to be constant (inlet pressure) in the diffusive term as the small pressure gradients in GDLs are negligible compared to the concentration gra-

dients; and lastly  $\mathbf{u}$  is the convective (superficial) velocity field, which is calculated by Darcy's Law in the anode, and assumed to be equal to the negative of the diffusive velocity of the inert specie,  $N_2$ , in the cathode. Note that the superficial velocity due to the pressure gradient is considered due to its convective effect in the anode, but diffusive effect due to the pressure gradient is neglected. Binary diffusion coefficients in mixtures are determined from [16]:

$$D_{ij} = 3.16 \times 10^{-8} \left( \frac{T^{1.75}}{p(v_i^3 + v_j^3)^2} \right) \left( \frac{1}{M_i} + \frac{1}{M_j} \right)^{1/2} \quad (2)$$

where,  $v_i$  is the molar volume of species  $i$ ,  $T$  is temperature, and  $M_i$  is the molecular weight of species,  $i$ .

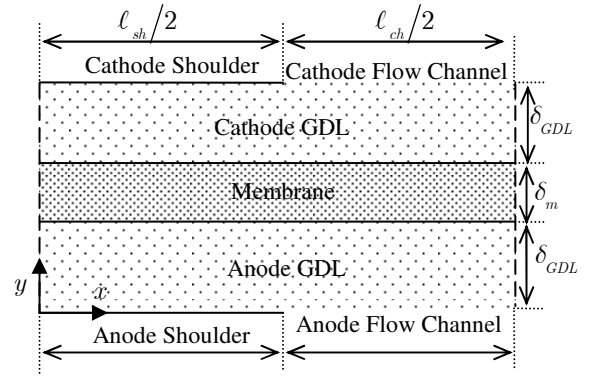


**FIGURE 1: TWO-DIMENSIONAL PEM FUEL CELL SECTION MODELED IN THIS WORK; DASHED LINES INDICATE SYMMETRY SURFACES.**

In the anode gas diffusion layer, gas flow is modeled as flow in the porous media to calculate the superficial velocity of the mixture as follows:

$$\mathbf{u}_a = -\frac{\kappa_{GDL}}{\mu_a} \nabla p \quad (3)$$

where,  $\kappa_{GDL}$ , is the permeability of the GDL,  $\mu_a$  is the viscosity of the mixture [16]. The velocity field in the anode gas diffusion layer is subject to continuity equation:

$$\frac{\partial}{\partial t}(\rho \epsilon_g) + \nabla \cdot \left( -\rho \frac{\kappa_{GDL}}{\mu} \nabla p \right) = 0 \quad (4)$$

### Transport of water in the membrane

Membrane water transport is due to (1) electro-osmotic drag (gradient of ionic potential), (2) diffusion (gradient of water concentration), and (3) gradient of membrane water pressure, leading to an average volumetric flux (superficial velocity) of the water in the membrane, based on the Schlogl velocity [13]:

$$\mathbf{v} = -\frac{\kappa_m}{\mu_w} \nabla p_w - V_{\text{H}_2\text{O}} c_{\text{SO}_3}^{(0)} D_\lambda \nabla \lambda - V_{\text{H}_2\text{O}} n_d \frac{\sigma_m}{F} \nabla \Phi_m \quad (5)$$

where,  $\kappa_m$  is the permeability of the membrane;  $\mu_w$  is the viscosity of the liquid water;  $V_{\text{H}_2\text{O}}$  is the molar volume of liquid water;  $p_w$  is the water pressure in the pores;  $c_{\text{SO}_3}^{(0)}$  is the molar density of sulfonic groups in the dry membrane;  $D_\lambda$  is the diffusion coefficient of water in the polymer membrane;  $n_d$  number of dragged water molecules per proton;  $\sigma_m$  is the ionic conductivity of the membrane, which is a function of  $\lambda$ ;  $F$  is the Faraday's constant; and  $\Phi_m$  is the ionic potential; and  $\lambda$  is the relative concentration of water with respect to the concentration of sulfonic groups in the dry membrane:

$$\lambda \equiv c_w / c_{\text{SO}_3}^{(0)} \quad (6)$$

A salient feature of our model, which is based on Biot's poroelasticity [12], is that the structural deformation of the polymer matrix dictates the water concentration of the membrane based on the assumption that water molecules are clustered as pores in the polymer matrix and the pore concentration is, in essence, given by the volumetric bulk strain itself. Thus, the molar concentration of water in the membrane is the ratio of the volumetric strain,  $\varepsilon_{kk}$ , to the molar volume of liquid water:

$$c_w = \frac{\varepsilon_{kk}}{V_{\text{H}_2\text{O}}} \quad (7)$$

Note that, in (6), the volumetric strain,  $\varepsilon_{kk}$ , is determined from the poroelastic stress-strain relationship [12].

In (5), the diffusion coefficient of water inside the polymer matrix of the membrane is given by [17]:

$$D_\lambda = 4.1 \times 10^{-10} \left( \frac{\lambda}{25} \right)^{0.15} \left[ 1 + \tanh \left( \frac{\lambda - 2.5}{4} \right) \right] \quad (8)$$

The last term on the right-hand-side in (5) corresponds to the superficial velocity of water due to ionic currents in the membrane. This term is calculated from the charge balance in the membrane.

As two terms of the Schlogl velocity in (5) can be determined from already calculated quantities, last unknown, which is water pressure,  $p_w$ , can be calculated from the conservation of water mass in the membrane:

$$\frac{\partial \rho_w \varepsilon_{kk}}{\partial t} + \nabla \cdot (\rho_w \mathbf{v}) = 0 \quad (9)$$

where  $\rho_w$  is water's density and constant.

For better accuracy of the numerical solution, the following manipulation akin to the use of a generalized potential is introduced:

$$g = A_p p_w + A_\lambda \lambda + A_\Phi \Phi_m \quad (10)$$

where,  $A_p = -\kappa_m / \mu$ ,  $A_\lambda = V_{\text{H}_2\text{O}} c_{\text{SO}_3}^{(0)} D_\lambda$  and  $A_\Phi = V_{\text{H}_2\text{O}} n_d \sigma_m / F$ .

Thus the velocity in (5) can be given in terms of the generalized potential as follows:

$$\mathbf{v} = -\nabla g + \tilde{\mathbf{v}} \quad (11)$$

where the  $\tilde{\mathbf{v}}$  term on the right-hand-side emerges from the  $\lambda$  dependence of each  $A$  term in (10). Furthermore, since  $\lambda$  is calculated from the volumetric strain, as in (7), one can determine  $\tilde{\mathbf{v}}$  from the volumetric strain:

$$\begin{aligned} \tilde{\mathbf{v}} &= p_w \nabla A_p + \lambda \nabla A_\lambda + \Phi_m \nabla A_\Phi \\ &= \left( p_w \frac{\partial A_p}{\partial \varepsilon_{kk}} + \lambda \frac{\partial A_\lambda}{\partial \varepsilon_{kk}} + \Phi_m \frac{\partial A_\Phi}{\partial \varepsilon_{kk}} \right) \nabla \varepsilon_{kk} = A_\varepsilon \nabla \varepsilon_{kk} \end{aligned} \quad (12)$$

Substituting (11) and (12) in (9), one obtains:

$$\frac{\partial \rho_w \varepsilon_{kk}}{\partial t} - \rho_w \nabla^2 g = -\rho_w \nabla \cdot (A_\varepsilon \nabla \varepsilon_{kk}) \quad (13)$$

where the term on the right-hand-side corresponds to a pseudo-source term which is determined from the bulk strain. Once the generalized potential,  $g$ , is determined, water pressure in the membrane can be obtained from (10).

### Deformation (force balance)

In the two-dimensional section of the PEM fuel cell, deformation of solid components, namely GDLs and the membrane is modeled using plane-strain formulation of the linear elasticity. Only in the membrane, the pore pressure due to its liquid content (water) is considered and added to the normal stress components akin to Biot's poroelasticity. The general stress-strain relationship used in modeling of the deformation is as follows [12]:

$$\sigma_{ij} = \frac{E}{(1+\nu)} \left( \varepsilon_{ij} + \frac{\nu}{1-2\nu} \varepsilon_{kk} \delta_{ij} \right) - \gamma \alpha p_w \delta_{ij} \quad (14)$$

where  $\sigma_{ij}$  are stress components for  $i, j = \{x, y, z\}$ ,  $E$  and  $\nu$  are the Young's modulus and the Poisson's ratio of the material,  $\varepsilon_{ij}$  are the strain components, which are zero when either  $i$  or  $j$  is  $z$ ,  $\varepsilon_{kk} = \varepsilon_{xx} + \varepsilon_{yy}$  is the volumetric bulk strain,  $\gamma$  is an indicator variable which is unity in the membrane and zero in the GDLs,  $\alpha$  is the Biot-Willis coefficient (unity for incompressible fluids such as water), and  $\delta_{ij}$  is the Kronecker's delta.

### Conservation of charge

Electrons are charge carriers in the GDLs. The conservation of charge based on the Ohm's Law is expressed as follows:

$$\nabla \cdot \mathbf{J}_e = 0, \quad \mathbf{J}_e = -\sigma_e \nabla \Phi_e \quad (15)$$

where,  $\sigma_e$  is the effective conductivity of the medium, and  $\Phi_e$  is the electric potential. Since the catalyst layers are projected onto membrane-GDL interfaces, there are no charge sources or sinks in the model geometry.

In the membrane, the charge carrier is the proton, for which the conservation of charge is given similar to that of electron to keep the current of the charged species in the same direction:

$$\nabla \cdot \mathbf{J}_+ = 0, \quad \mathbf{J}_+ = -\sigma_m \nabla \Phi_m \quad (16)$$

where  $\Phi_m$  is the ionic potential and  $\sigma_m$  is the effective conductivity of the membrane, which is water content dependent [18]:

$$\sigma_m = \left( -0.326 + 0.514 \lambda \right) \exp \left( 1268 \left( \frac{1}{303} - \frac{1}{T} \right) \right) \quad (17)$$

### Boundary conditions

**For mass fractions in the Maxwell-Stefan equation:** At interfaces between the GDLs and gas flow channels, convection mass transfer in a laminar boundary layer is assumed due to laminar flow in gas flow channels, and implemented as follows:

$$\rho w_i \left[ \mathbf{u} - \sum_{j \neq i} D_{ij} \nabla x_j \right] \cdot \mathbf{n} = h_{i,ch} (w_i - w_{i,ch}) \quad (18)$$

where  $\rho$  is the density of the mixture in the GDL,  $\mathbf{n}$  is the surface normal,  $w_{i,ch}$  is the mass fraction of the  $i^{\text{th}}$  specie in the flow channel, and  $h_{i,ch}$  is the mass transfer coefficient determined from the Sherwood number,  $Sh$ , for gas flow in a square-cross-section, which is constant for laminar flow [16]:

$$Sh = \frac{h_{i,ch} \ell_{ch}}{D_{i,mix}} = 2.7 \quad (19)$$

In (19),  $\ell_{ch}$  is the width of the channel, and  $D_{i,mix}$  is the diffusion coefficient of the  $i^{\text{th}}$  specie in the gas mixture, namely  $D_{\text{H}_2\text{-H}_2\text{O}}$ ,  $D_{\text{O}_2\text{-air}}$  and  $D_{\text{H}_2\text{O-air}}$  for  $\text{H}_2$ ,  $\text{O}_2$  and  $\text{H}_2\text{O}$  vapor respectively.

At the membrane-GDL interfaces, we have flux boundary conditions to mimic the sinks and sources in catalyst layers, which are equal to rates of consumption of the species:

$$\rho w_i \left[ \mathbf{u} - \sum_{j \neq i} D_{ij} \nabla x_j \right] \cdot \mathbf{n} = \frac{M_i i_{\{a,c\}}}{n_i F} \quad (20)$$

In (20),  $\mathbf{u}$  is given by (3) for anode and the negative of the diffusive velocity of  $\text{N}_2$  in the cathode,  $M_i$  is the molar mass of the  $i^{\text{th}}$  specie;  $n_i$  is the stoichiometric coefficient of each species and negative for  $\text{H}_2$  and  $\text{O}_2$  and positive for  $\text{H}_2\text{O}$ ; and  $i_a$  and  $i_c$  are anode and cathode exchange currents respectively, and given by Butler-Volmer's expression [19]:

$$i_{\{a,c\}} = \left( S_a i_0^{ref} \right)_{\{a,c\}} \delta_{CL} \left( \frac{c_{\{\text{H}_2, \text{O}_2\}}}{c_{\{\text{H}_2, \text{O}_2\}}^{ref}} \right)^b \times \left[ \exp \left( \beta_{\{a,c\}} \frac{F}{RT} \eta_{\{a,c\}} \right) - \exp \left( -\beta_{\{a,c\}} \frac{F}{RT} \eta_{\{a,c\}} \right) \right] \quad (21)$$

In (21),  $(S_a i_0^{ref})_{\{a,c\}}$  is the product of the surface area of the catalyst and the reference current density for anode and cathode respectively; catalyst layers' thickness,  $\delta_{CL}$ , is the same for both anode and the cathode;  $c_{\text{H}_2}^{ref}$  and  $c_{\text{O}_2}^{ref}$  are reference concentrations of  $\text{H}_2$  and  $\text{O}_2$  at the anode and cathode;  $b$  is 0.5 for  $\text{H}_2$  and unity for  $\text{O}_2$ ;  $R$  is the universal gas constant,  $\beta_{\{a,c\}}$  are coefficients, and  $\eta_{\{a,c\}}$  are overpotentials at the anode and cathode respectively, and given by:

$$\eta_{\{a,c\}} = \Phi_e - \Phi_m - \Phi_{0,\{a,c\}} \quad (22)$$

In (22),  $\Phi_e$  and  $\Phi_m$  are electric and ionic potentials given by (15) and (16),  $\Phi_{0,a}$  is the open circuit potential at the anode, which is taken as 0, and  $\Phi_{0,c}$  is the open circuit potential at the cathode and given by [20]:

$$\Phi_{0,c} = 1.23 - 0.83 \times 10^{-3} (T - 298) \quad (23)$$

Fluxes of all species are set to zero at the symmetry surfaces of the 2D geometry in the normal directions.

**For anode GDL pressure in (4):** The superficial velocity at the anode GDL is calculated from (3) by solving (4). The boundary conditions for the anode gas pressure are specified at the GDL-gas-flow-channel interface as the anode flow channel pressure,  $p_{a,ch}$ , which is very close to the inlet pressure:

$$p = p_{a,ch} \quad (24)$$

At the interface between the membrane and the anode GDL, the superficial velocity of the mixture can be determined from the reaction of  $\text{H}_2$  and the electro-osmotic drag of water into the membrane:

$$\mathbf{u} \cdot \mathbf{n} = -\frac{i_a M_{\text{H}_2}}{2F \rho_a} + \frac{\rho_w v_m}{\rho_a} \quad (25)$$

where  $v_m$  is the y-component of the velocity of the flow in the membrane.

At the symmetry surfaces and GDL-shoulder boundary, the velocity is set to zero.

**For the conservation of membrane water:** Equation (13) gives the conservation of mass for the membrane water by means of a variable transformation that introduces a function which combines all the driving forces that dictate the water transport in the membrane for which the volumetric flux (superficial velocity) is given by (5). In typical diffusive models of the membrane water transport, non-equilibrium boundary conditions are deemed appropriate, and successfully implemented by several authors. In addition to the diffusion, the effect of the electro-osmotic drag is also included [13]. Moreover, recently, Nazarov and Promislow used non-equilibrium boundary conditions for the chemical potential of the membrane water, which included its activity and pressure [11]. Based on the experimental results of Ge et al [21], diffusive forces contributing to the transport of the membrane water are implemented here. Moreover, the electro-osmotic drag is included due to the effect of the ionic potential of the membrane on the transport of water. Lastly, the pressure imbalance between the membrane and the GDL is included assuming Poiseuille flow through the pores of the membrane near the interface where the pressure imbalance between the GDL and the membrane network is effective. Combining these three effects that contribute to the volumetric flux given by (5), we have the following boundary condition for the membrane-anode-GDL interface:

$$\mathbf{u} \cdot \mathbf{n} = \frac{n_d V_{\text{H}_2\text{O}}}{F} (\mathbf{J}_+ \cdot \mathbf{n}) + k_\lambda V_{\text{H}_2\text{O}} c_{\text{SO}_3}^{(0)} (\lambda - \lambda_a^*) + k_p (p_w + p_{\text{cap}} - p_a) \quad (26)$$

In (26),  $\mathbf{n}$  is the surface normal;  $n_d$  is electro-osmotic coefficient, which is a function of  $\lambda$ ;  $\mathbf{J}_+$  is the ionic flux, which is defined in (16);  $k_\lambda$  is mass transfer coefficient;  $\lambda_a^*$  is equilibrium concentration for the anode water activity;  $k_p$  is the pressure coefficient; and  $p_w$ ,  $p_{\text{cap}}$  and  $p_a$  are membrane water, capillary pressure and anode pressures respectively.

The mass transfer coefficient is experimentally calculated by Ge et al [21]:

$$k_\lambda = \begin{cases} 1.14 \times 10^{-5} f_V \exp(2416(1/T_0 - 1/T)), & \lambda < \lambda^* \\ 4.59 \times 10^{-5} f_V \exp(2416(1/T_0 - 1/T)), & \lambda > \lambda^* \end{cases} \quad (27)$$

where  $f_V = \lambda V_{\text{H}_2\text{O}} / (\lambda V_{\text{H}_2\text{O}} + V_m)$  is the volume fraction of the water in the membrane,  $V_m$  is the volume fraction of the dry

membrane and  $\lambda^*$  is the equilibrium concentration at the boundary, which is given by [21]:

$$\lambda^* = \begin{cases} 0.043 + 17.81 a - 39.85 a^2 + 36 a^3, & T = 303\text{K} \\ 0.3 + 10.8 a - 16 a^2 + 14.1 a^3, & T = 353\text{K} \end{cases} \quad (28)$$

The pressure coefficient is calculated from the Poiseuille flow assumption in the pores near the interface, i.e.

$$v_{\text{pore}} = \frac{r_{\text{pore}}^2}{8\mu\ell_{\text{pore}}} (p_{\text{pore}} - p_{\text{out}}) = k_p (p_w + p_{\text{cap}} - p_{\{a,c\}}) \quad (29)$$

where,  $r_{\text{pore}}$  and  $\ell_{\text{pore}}$  are the pore radius and length respectively and are both about 1 nm [22], thus, yielding  $k_p \approx 10^{-7} \text{ m-s-N}^{-1}$ . Note that, arguably equilibrium pressure boundary condition is more appropriate for water pressure, however, akin to models that use chemical potential and for consistency with other gradient terms in (26), we incorporate the non-equilibrium model. Moreover, a relatively large  $k_p$  can ensure equilibrium pressure, however it causes numerical instabilities in our model.

The capillary pressure,  $p_{\text{cap}}$ , is given by the Young-Laplace equation, e.g. [23]:

$$p_{\text{cap}} = \frac{2\sigma_s \cos \theta_c}{r_{\text{pore}}} \quad (30)$$

where  $\sigma_s$  is the surface tension,  $\theta_c$  is the contact angle (which is about 93 degrees for Nafion and water [11]), and the pore radius,  $r_{\text{pore}}$  depends on the bulk strain and the specific surface area of the pores,  $S_{\text{pore}}$  [10]:

$$r_{\text{pore}} = \max \left( \frac{2\varepsilon_{kk}}{S_{\text{pore}}}, r_{\text{LB}} \right) \quad (31)$$

In the model, a lower bound  $r_{\text{LB}} = 0.1 \text{ nm}$  is used for  $r_{\text{pore}}$  to avoid unphysical results.

At the membrane-cathode-GDL interface, similarly to the conditions at the anode side, we have:

$$\left( \mathbf{u} + \frac{V_{\text{H}_2\text{O}}}{2F} \mathbf{J}_+ \right) \cdot \mathbf{n} = \frac{n_d V_{\text{H}_2\text{O}}}{F} (\mathbf{J}_+ \cdot \mathbf{n}) + k_\lambda V_{\text{H}_2\text{O}} c_{\text{SO}_3}^{(0)} (\lambda - \lambda_c^*) + k_p (p_w + p_{\text{cap}} - p_c) \quad (32)$$

In (32), compared to (29), we also have the source term, which corresponds to the generation of water in the cathode catalyst layer. Other specific variables in (32) are,  $\lambda_c^*$  is equilibrium concentration for the anode water activity; and  $p_c$  is the cathode pressure. In our model, we have the same anode and

cathode pressures, which constitute a reference to the membrane water pressure and, thus, taken to be zero.

For other boundary conditions at the symmetry surfaces, the velocity is set to zero.

**For deformation:** Equation (14) is solved in the displacement form with the actual displacement vector,  $[\xi, \zeta]^T$ , for which the strain-tensor components are:

$$\varepsilon_x = \frac{\partial \xi}{\partial x}, \quad \varepsilon_y = \frac{\partial \zeta}{\partial y}, \quad \varepsilon_{xy} = \frac{1}{2} \left( \frac{\partial \xi}{\partial y} + \frac{\partial \zeta}{\partial x} \right) \quad (33)$$

The 2D PEM fuel section shown in Figure 1 is assumed to be fixed in the y-direction at the bottom but free to move in the x-direction, i.e.:

$$\zeta(x < \ell_{sh} / 2, 0) = 0 \quad (34)$$

Left side is fixed in the x-direction but can freely deform in the y-direction:

$$\xi(0, y) = 0 \quad (35)$$

The right side can freely move in the y-direction, but can move in the x-direction only as much as the bottom surface (edge) does:

$$\zeta(\ell_{tot}, 0) = 0, \quad (36)$$

and

$$\xi(\ell_{tot}, y) = \xi(\ell_{tot}, y) \quad (37)$$

where  $\ell_{tot} = (\ell_{sh} + \ell_{ch}) / 2$  is the total width of the PEM fuel section.

Lastly, top of the section is free to move in the y-direction but subject to constant compressive load due to clamping. Similar boundary conditions are also used in structural analysis of PEM fuel cell cross-sections [2,3,9].

**For conservation of charge:** The electric potential is set to ground at the anode shoulder boundary of the anode GDL:

$$\Phi_e(x, 0) = 0 \quad (38)$$

At the cathode shoulder, the load current density,  $J_{cell}$ , is imposed:

$$\mathbf{J}_e(x, 2\delta_{GDL} + \delta_m) \cdot \mathbf{n} = J_{cell} \quad (39)$$

At interfaces between the membrane and GDLs, electric and ionic currents are given by the exchange currents,  $i_{\{a,c\}}$ , which are defined in (21). Thus, we have:

$$\mathbf{J}_e(x, \delta_{GDL}) \cdot \mathbf{n}_c = -i_a \quad (40)$$

$$\mathbf{J}_e(x, \delta_{GDL} + \delta_m) \cdot \mathbf{n}_c = -i_c \quad (41)$$

$$\mathbf{J}_m(x, \delta_{GDL}) \cdot \mathbf{n}_m = i_a \quad (42)$$

and

$$\mathbf{J}_m(x, \delta_{GDL} + \delta_m) \cdot \mathbf{n}_m = i_c \quad (43)$$

In (39) – (43),  $\mathbf{n}_m$ ,  $\mathbf{n}_c$  and  $\mathbf{n}_a$  are surface normals with respect to the membrane, cathode GDL and anode GDL respectively.

## Initial Conditions

In simulations, steady-state conditions are used as initial conditions during transients; parameters that correspond to each simulation are explicitly given in the results section.

## NUMERICAL APPROACH

Governing equations, which are given by (1), (4), (10), and (13) – (16) subject to boundary conditions, which are given in detail above are solved using a commercial multiphysics finite-element code, COMSOL [14], for steady-state and transients. In total of 1854 triangular elements with quadratic Lagrange shape functions are used; total number of degrees of freedom is 18652. Numerical solution does not particularly depend on the mesh selection more than assigned tolerances. A direct solver, UMFPAK, with undamped Newton and relative tolerance of  $10^{-9}$  is used in steady-state and time-dependent simulations. For the latter, the 5<sup>th</sup> order variable time-step backward differencing is also invoked. Similarly to the strategy outlined in [15], steady-state solutions are obtained from ‘bootstrapping’ of each multiphysics component.

A typical steady state simulation takes a few minutes on a 2.2 GHz CoreDuo, Windows XP-SP2, 3GB RAM laptop. A transient simulation, which follows a rapid ramp takes between 10 minutes and 1 hour depending on the conditions of the transient.

## RESULTS

In Table 2, typical PEM fuel cell model parameters are listed with references where applicable.

Following averages are used among the performance metrics that are used in comparisons of simulation results:

**Cell voltage:** At the cathode GDL interface with the shoulder, where the electric load boundary conditions are applied the electric potential is averaged over the surface and given by:

$$V_{cell} = \frac{2}{\ell_{sh}} \int_0^{\ell_{sh}/2} \Phi_e dx \quad (44)$$

**Average membrane water content:** Number of water molecules per sulfonic group in the membrane is averaged over the entire membrane:

$$\lambda_{av} = \frac{1}{V_{mem}} \int_{V_{mem}} \lambda dV \quad (45)$$

**Von Mises stress:** To quantify the stress levels in the fuel cell components one can use the von Mises stress, which is defined for plane-strain formulation as follows:

$$\sigma_{vM} = \left( \sigma_x^2 + \sigma_y^2 + \sigma_z^2 - \sigma_x \sigma_y - \sigma_x \sigma_z - \sigma_y \sigma_z + 3\sigma_{xy}^2 \right)^{\frac{1}{2}} \quad (46)$$

where  $\sigma_i$  are normal stress components and  $\sigma_{xy}$  is the shear stress on the x-y plane.

In simulations, cell load current density, relative humidity of the anode and cathode inlets,  $RH_{\{a,c\}}$ , and the clamping force applied to the shoulder part of the cathode GDL are used as simulation variables. Unless otherwise noted, the base case values of these variables are given in Table 3.

### Steady-state results

In order to verify that the model captures the essential features of a typical PEM fuel cell operation; a typical polarization curve for the base case conditions is obtained from the model and shown in Figure 2. Activation losses followed by Ohmic and concentration losses are identifiable in the polarization curve. The cell voltage is obtained from (44). Note that, catalyst loading variables are estimated to have a realistic polarization curve that reflects a typical PEM fuel cell operation within the range of values available in the literature.

Average membrane water content for the base case conditions is plotted against the load density in Figure 3. As expected, the membrane water content increases with increasing water production at the cathode.

Even though the ionic currents in the membrane are almost uniform and only in the y-direction, electric currents originating from the shoulders go tangentially under the gas flow channels where insulation boundary conditions are imposed (Figs. 4a-d). Electric and ionic currents peak in the portion that aligns with shoulders in the x-direction for low currents (Figs. 4a-c), and shift towards the channel at high currents (Fig. 4d)

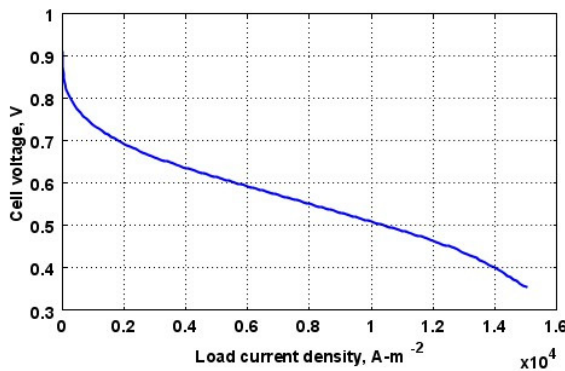


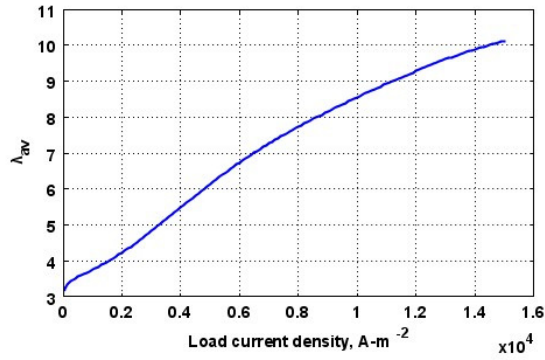
FIGURE 2: POLARIZATION CURVE FOR THE BASE CASE.

TABLE 2: MATERIAL PROPERTIES AND THE BASE OPERATING CONDITIONS.

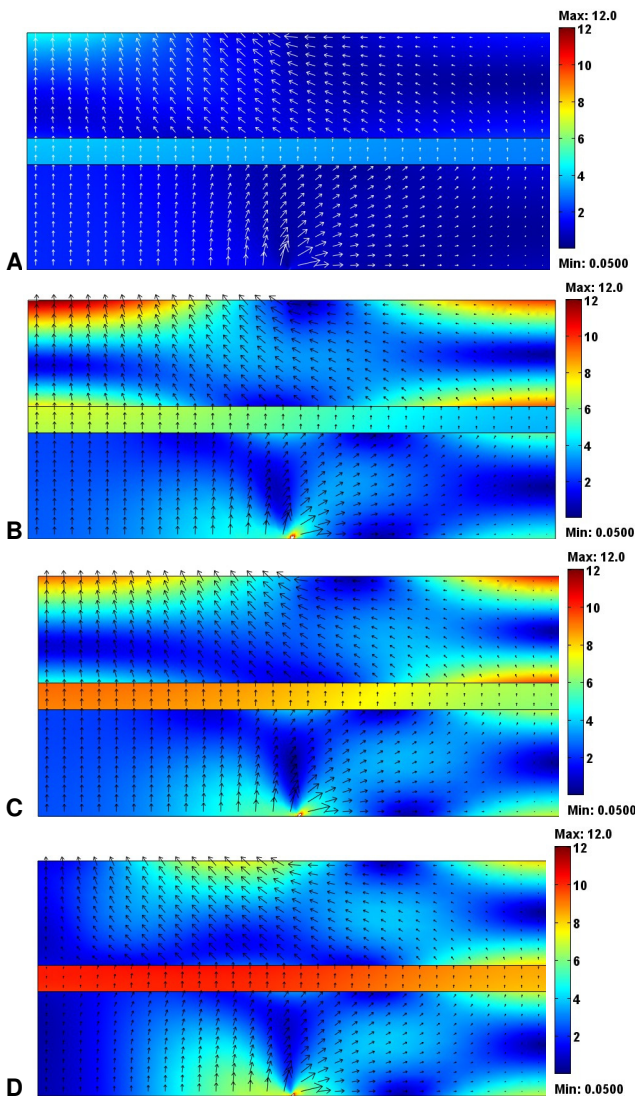
Property, symbol	Value
Cell operating temperature, $T_0$	353 K
Faraday's constant, $F$	96487 C·mol <sup>-1</sup>
Universal gas constant, $R$	8.31 J·kg <sup>-1</sup> ·mol <sup>-1</sup>
Molar volume of oxygen, $v_{O_2}$	16.6 × 10 <sup>-6</sup> m <sup>3</sup> ·mol <sup>-1</sup>
Molar volume of nitrogen, $v_{N_2}$	17.9 × 10 <sup>-6</sup> m <sup>3</sup> ·mol <sup>-1</sup>
Molar volume of water vapor, $v_{H_2O}$	12.7 × 10 <sup>-6</sup> m <sup>3</sup> ·mol <sup>-1</sup>
Porosity of GDLs, $\epsilon_g$	0.6
Permeability of GDLs, $\kappa_{GDL}$	10 <sup>-13</sup> m <sup>2</sup>
Anode and cathode inlet pressures, $P_{\{a,c\},in}$	{200,200} kPa
Anode and cathode gas viscosities, $\mu_{\{a,c\}}$ [calc.]	{2.08,3} × 10 <sup>-5</sup> Pa·s
Permeability of the membrane, $\kappa_m$ [11]	(0.4 + 0.074 $\lambda^2$ ) × 10 <sup>-20</sup> m <sup>2</sup>
Active area of anode and cathode catalyst layers, $(S_{a_0}^{ref})_{\{a,c\}}$ [4, est.]	{10 <sup>11</sup> ,30} A·m <sup>-3</sup>
Anode and cathode coefficients, $\beta_{\{a,c\}}$ [4]	{2,1}
H <sub>2</sub> and O <sub>2</sub> reference concentrations, $c_{\{H_2,O_2\}}^{ref}$ [25]	{56.4,3.39} mol·m <sup>-3</sup>
Electro-osmotic drag coefficient, $n_d$ [21]	1.2
Electric conductivity of GDLs, $\sigma_e$	100 S·m
Young's modulus of GDLs, $E_{GDL}$	10 GPa
Poisson's ratio of GDLs, $\nu_{GDL}$	0.25
Young's modulus of membrane, $E_m$ [11]	63 MPa
Poisson' ratio of the membrane, $\nu_m$	0.25
Specific surface of membrane pores, $S_{pore}$ [10]	2.1 × 10 <sup>8</sup> m <sup>2</sup> ·m <sup>-3</sup>
Surface tension of water, $\sigma_s$ [11]	0.072 N·m <sup>-1</sup>

TABLE 3. BASE CASE CONDITIONS USED IN SIMULATIONS

Property	Value
Anode and cathode inlet relative humidity, $RH_{\{a,c\}}$	{0.5, 0.5}
Clamping force	1 MPa



**FIGURE 3: AVERAGE MEMBRANE WATER CONCENTRATION PER SULFONIC GROUP AS A FUNCTION OF LOAD CURRENT FOR THE BASE CASE.**



**FIGURE 4: VON MISES STRESS DISTRIBUTION AND CURRENT VECTORS IN THE PEM FUEL CELL SECTION FOR  $J_{cell} = 2000, 5000, 10000,$  AND  $15000 \text{ A-M}^{-2}$  (A-D).**

Effect of the clamping pressure on the average membrane water concentration (per sulfonic group) is shown in Figure 5 for  $RH_a = RH_c = 0.5$  and  $J_{cell} = 5000 \text{ A-m}^{-2}$ . As the compression increases membrane's water content decreases as if the compression "squeezes" the membrane similarly to a sponge to reduce its water content. Similar behavior is observed by the model developed by [11]. Cell voltage does not vary significantly with the clamping pressure since our model does not include contact resistances, which are very important in the overall performance of the PEM fuel cell as addressed elsewhere, e.g. [24].

Moreover, distribution of the membrane water content becomes more uniform as the compression increases as depicted in Figure 6, where  $\lambda$  distribution at the anode-side of the membrane is plotted with respect to x-coordinate and varying magnitudes of the clamping pressure. The squeezing effect of the compression is more pronounced in flattening of  $\lambda$  distribution (Fig. 6) than the overall slight decrease of the water content (Fig. 5).

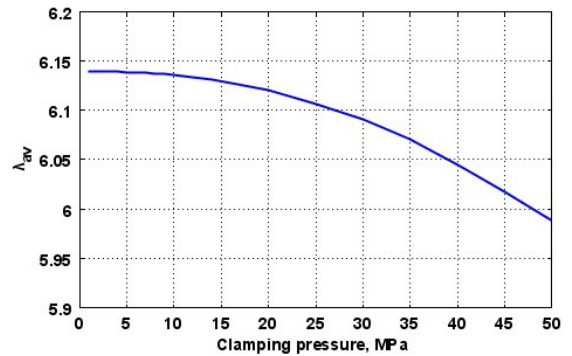


**FIGURE 5: AVERAGE WATER CONCENTRATION PER SULFONIC GROUP IN THE MEMBRANE AS A FUNCTION OF CLAMPING PRESSURE FOR  $J_{cell} = 5000 \text{ A-M}^{-2}$ .**

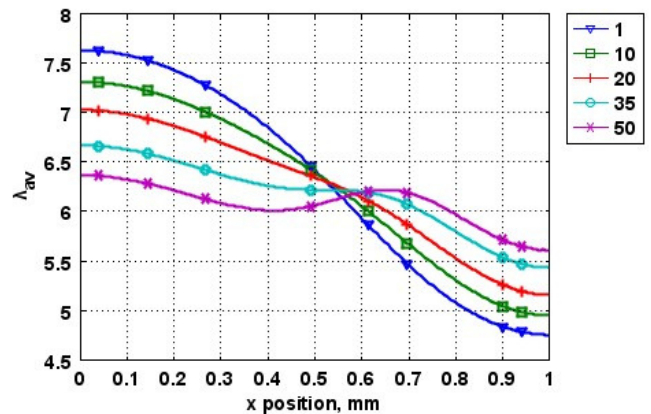


**FIGURE 6: WATER CONCENTRATION (PER SULFONIC GROUP) PROFILE AT THE ANODE-MEMBRANE INTERFACE FOR CLAMPING PRESSURES OF 1, 10, 20, 30 AND 50 MPa.**



## **Transient results**

### **Load transient**

In Figure 7, transient cell voltage is plotted against time in response to ramping up of the load current density from 2000 to 7000 A-m<sup>-2</sup> at t = 10 s for 0.1 seconds. The sudden drop of the cell voltage, which is due to load increase is followed by a recovery yielding an undershoot behavior, which is observed in experimental studies, e.g. [1], and in transient models, e.g. [25].

Figure 8 shows the variation of  $\lambda_{av}$  during the load transient. It is clear that conductivity of the membrane increases due to increasing  $\lambda_{av}$ , and leads to the recovery of the cell voltage observed in Figure 7. The response of  $\lambda_{av}$  resembles to that of a typical first order system.

In Figure 9, membrane water pressure at the cathode-side and x-positions of 0 and 1mm are plotted against time for the load transient. At x = 0, which aligns with the center of the shoulder, water pressure increases from about 6.5 MPa to 13 MPa during the transient and stabilizes. However at x = 1mm, where aligns with the center of the flow channel, final pressure is smaller than that of at x = 0 mm. Water pressure increase is expected due to increasing production of water.

Lastly, the Mises stresses at the anode and cathode sides of the membrane and at the midplane of the shoulder (x = 0) are shown in Figure 10 for the load transient. Increase of stress on the cathode-side of the membrane is more pronounced than the one on the anode-side due to the production of water on the cathode.

### **Anode humidity transient**

For  $J_{cell} = 2000$  A-m<sup>-2</sup>, RH<sub>c</sub> = 0.5 and  $F_{clamp} = 1$  MPa, anode relative humidity is increased to 1 from 0.1 at t = 10 s with a ramp in 0.1 seconds. Membrane water content increases as expected following the increase of the relative humidity of the anode inlet as shown in Figure 11.

Response of the cell voltage is shown in Figure 12. As the membranes conductivity increases, so does the cell voltage albeit small.

Mises stresses at the anode and cathode side of the membrane at x = 0 (shoulder mid-plane) are shown in Figure 13. Cathode side stress is larger throughout the transient. However despite that the stress increases at the anode side at the beginning of the transient, stress at the cathode side has the opposite tendency, which recovers only after the transient progresses.

### **Cathode humidity transient**

Cathode relative humidity is increased from 0.1 to 1.0 at t = 10 seconds with a ramp that lasts 0.1 seconds for RH<sub>a</sub> = 0.5,

$J_{cell} = 2000$  A-m<sup>-2</sup>, and  $F_{clamp} = 1$  MPa. The response of the  $\lambda_{av}$  resembles to that of a first order response (nearly exponential) as shown in Figure 14. Cell voltage does not change significantly (not shown here).  $\sigma_{vM}$  at the anode and cathode sides of the membrane and the symmetry surface of the shoulders increase with the transient (Fig. 15). Although  $\sigma_{vM}$  at the cathode side is larger than the one at the anode side before the transient, anode side stress becomes larger after the transient. However the difference between the two is small.

## **CONCLUSIONS**

A two-dimensional time-dependent model of a PEM fuel cell cross-section that contains membrane and gas diffusion layers is developed here. Transport of gas species in gas diffusion layers, conservation of charge, linear elastic deformation of GDLs, poroelastic deformation of the membrane, and water transport in the membrane are considered in the model, which is, then, used to analyze the coupled effect of compressive clamping pressure and transport of water in the membrane.

The model captures the typical characteristics of a PEM fuel cell and membrane water transport, and elucidates the effect of clamping pressure on the performance of the fuel cell and the effect of operating conditions on the stresses that develop in the membrane and GDL.

In particular, increasing load current density results in higher stresses in the membrane more than 10 times of the pressure due to clamping forces for load density of 15000 A-m<sup>-2</sup>. Similarly, increasing clamping pressure ‘squeezes’ the membrane resulting in considerable water loss and flatter water distribution within the membrane.

During load transients, cell voltage demonstrates the typical undershoot (for increasing load) behavior; and membrane stresses increase in the portion that aligns with the shoulders’ symmetry plane (middle).

RH transients of the anode and cathode do not cause significant variation in the cell voltage, but affect the amount of water in the membrane, and result in increasing membrane stresses.

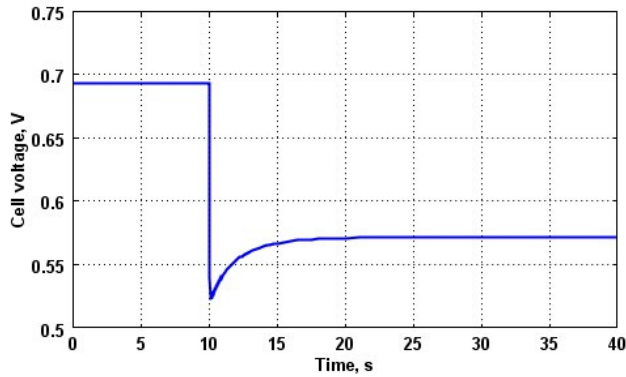


FIGURE 7: CELL VOLTAGE AS A FUNCTION OF TIME IN RESPONSE TO A FAST RAMP IN LOAD CURRENT DENSITY FROM 2000 TO 7000 A-M<sup>-2</sup> AT T=10 S WITH A DURATION OF 0.1 S.

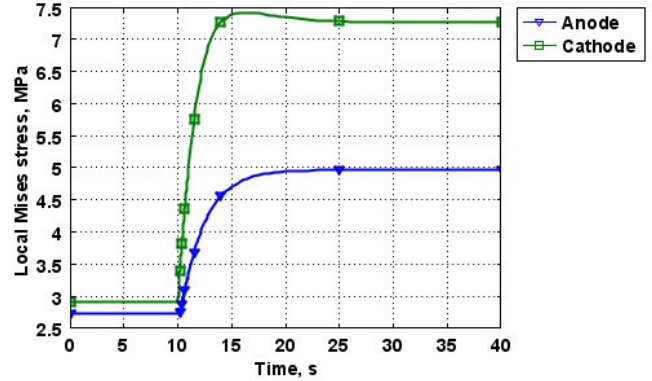


FIGURE 10: MISES STRESS AT THE ANODE (BLUE LINE SQUARE MARKERS) AND CATHODE (GREEN LINE TRIANGLE MARKERS) SIDES OF THE MEMBRANE DURING THE LOAD TRANSIENT.

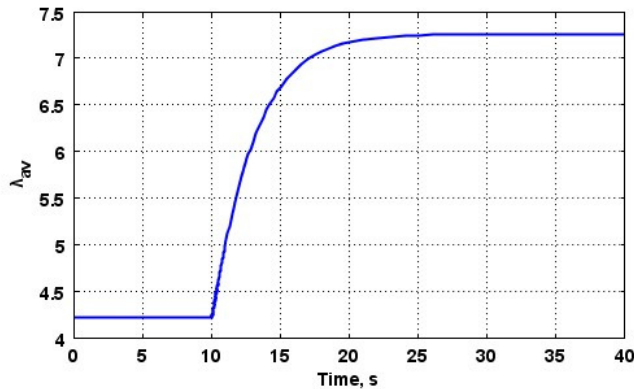


FIGURE 8: AVERAGE WATER CONCENTRATION PER SULFONIC GROUP IN THE MEMBRANE AS A FUNCTION OF TIME IN RESPONSE TO RAMP LOAD CURRENT DENSITY FROM 2000 TO 7000 A-M<sup>-2</sup> AT T=10 WITH THE DURATION OF 0.1 S.

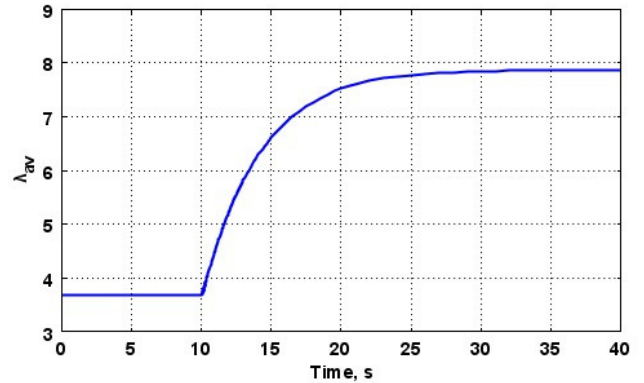


FIGURE 11: AVERAGE WATER CONCENTRATION PER SULFONIC GROUP IN THE MEMBRANE AS A FUNCTION OF TIME IN THE ANODE-RH TRANSIENT.

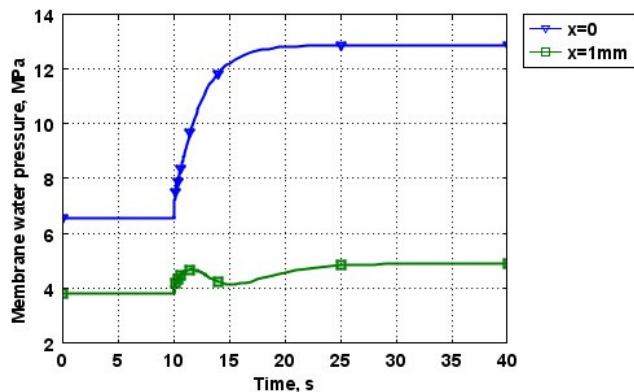


FIGURE 9: WATER PRESSURE IN THE MEMBRANE AT THE MEMBRANE-CATHODE INTERFACE AND X=0 (UNDER THE SHOULDER), AND X=1 MM (UNDER THE CHANNEL) DURING THE LOAD TRANSIENT.

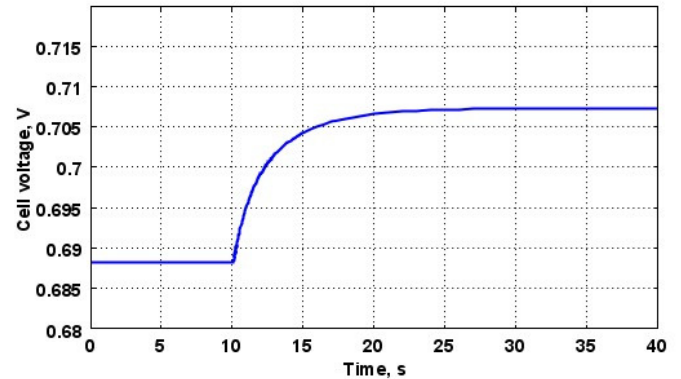


FIGURE 12: CELL VOLTAGE AS A FUNCTION OF TIME IN RESPONSE TO THE RAMP CHANGE OF ANODE RH FROM 0.1 TO 1.0 AT T=10 S WITH THE DURATION OF 0.1 S.

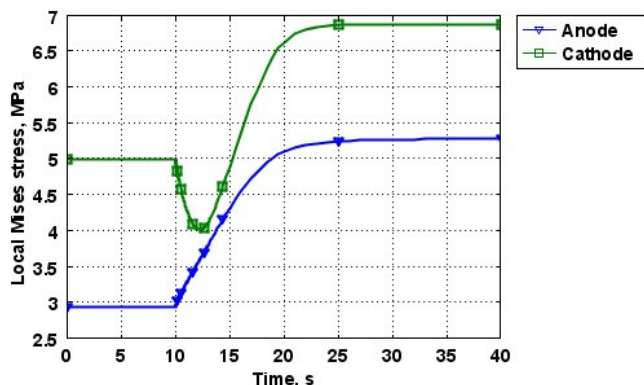


FIGURE 13: MISES STRESS AT THE ANODE (BLUE LINE SQUARE MARKERS) AND CATHODE (GREEN LINE TRIANGLE MARKERS) SIDES OF THE MEMBRANE DURING THE ANODE-RH TRANSIENT.

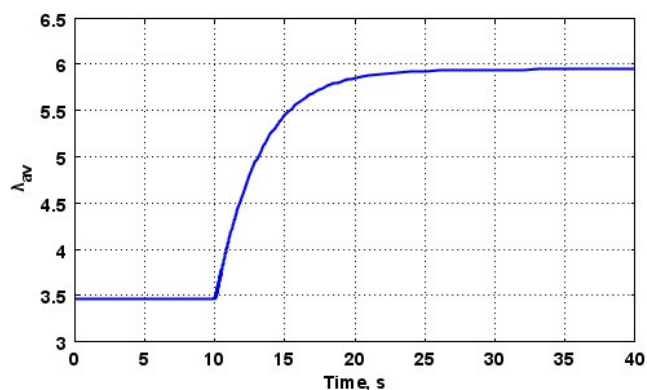


FIGURE 14: AVERAGE WATER CONCENTRATION PER SULFONIC GROUP IN THE MEMBRANE AS A FUNCTION OF TIME IN THE CATHODE-RH TRANSIENT.

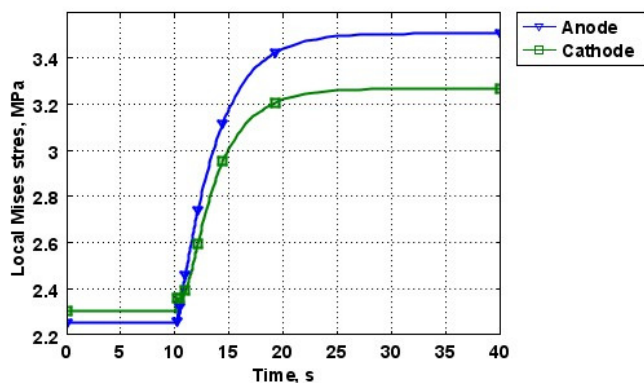


FIGURE 15: MISES STRESS AT THE ANODE (BLUE LINE SQUARE MARKERS) AND CATHODE (GREEN LINE TRIANGLE MARKERS) SIDES OF THE MEMBRANE DURING THE CATHODE-RH TRANSIENT.

## ACKNOWLEDGMENTS

This work is partially supported by The Scientific and Technological Research Council of Turkey (TUBITAK).

Author is currently on sabbatical leave in The University of Michigan in Ann Arbor, and expresses his gratitude for resources provided by Professor Anna Stefanopoulou and the Mechanical Engineering Department.

## REFERENCES

- [1] Benziger, J., Chia, E., Moxley, J.F., Kevrekidis, I.G., 2005, "The dynamic response of PEM fuel cells to changes in load," *Chem. Eng. Sci.*, **60**, pp. 1743-1759.
- [2] Kusoglu, A., Karlsson, A.M, Santare, M., Cleghorn, S., Johnson, W.B., 2007, "Mechanical behavior of fuel cell membranes under humidity cycles and effect of swelling anisotropy on the fatigue stresses," *J. Power Sources*, **170**, pp. 345-358.
- [3] Solasi, R., Zou, Y., Huang, X., Reifsnider, K., Condit, D., 2007, "On mechanical behavior and in-plane modeling of constrained PEM fuel cell membranes subjected to hydration and temperature cycles", *J. Power Sources*, **167**, pp. 366-377.
- [4] Berning, T., Djilali, N., 2003, "A 3D, multiphase, multicomponent model of the cathode and anode of a PEM fuel cell," *J. Electrochem. Soc.*, **150**(12), pp. A1589-A1598.
- [5] Pasaogullari, U., Wang, C.-Y., 2005, "Two-phase modeling and flooding prediction of polymer electrolyte fuel cells," *J. Electrochem. Soc.*, **152**(2), pp. A380-A390.
- [6] Serincan, M.F., Yesilyurt, S., 2007, "Transient analysis of Proton Electrolyte Membrane Fuel Cells (PEMFC) at startup and shutdown," *Fuel Cells*, **7**(2), pp. 118-127.
- [7] Shah, A.A., Kim, G.S., Sui, P.C., Harvey, D. 2007, "Transient non-isothermal model of a polymer electrolyte fuel cell," *J. Power Sources*, **163**, pp. 793-806.
- [8] Zhou, P., Wu, C.W., Ma, G.J., 2007, "Influence of clamping force on the performance of PEMFCs," *J. Power Sources*, **163**, pp. 874-881.
- [9] Tang, Y., Santare, M.H., Karlsson, A.M., Cleghorn, S., Johnson, W.B., 2006, "Stresses in Proton Exchange Membranes due to hygro-thermal loading," *J. Fuel Cell Sci. Technol.*, **3**, pp. 119-124.
- [10] Choi, P., Jalani, N.H., Datta, R., 2005, "Thermodynamics and proton transport in nafion I: Membrane swelling, sorption, and ion-exchange equilibrium." *J. Electrochem. Soc.*, **152**(3), pp. E84-E89.
- [11] Nazarov, I., Promislow, K., 2007, "The impact of membrane constraint on PEM fuel cell water management," *J. Electrochem. Soc.*, **154**(7), B623-B630.
- [12] Wang, H.F., 2000, *Theory of Linear Poroelasticity with Applications to Geomechanics and Hydrogeology*, Princeton University Press, Princeton, New Jersey.
- [13] Eikerling, M., Kharkats, Y.I, Kornyshev, A.A., Volkovich, Y.M., 1998, "Phenomenological theory of electro-osmotic effect and water management in polymer electrolyte proton-

- conducting membranes,” *J. Electrochem. Soc.*, **145**(8), pp. 2684-2699.
- [14] COMSOL, 2008, “COMSOL Multiphysics User Guide”, COMSOL A.B., Stockholm.
- [15] Yesilyurt, S, 2007, “Three-dimensional simulations of transient response of PEM fuel cells,” in *Proc. of IMECE2007*, Seattle, Washington.
- [16] Bird, R.B., Stewart, W.E., Lightfoot, E.N., 2002, *Transport Phenomena*, 2<sup>nd</sup> ed, Wiley, New York.
- [17] Kulikovskiy, A.A., 2003, “Quasi-3D modeling of water transport in polymer electrolyte fuel cells,” *J. Electrochem. Soc.*, **150**(11), A1432-A1439.
- [18] Springer, T.E., Zawodzinski, T.A., and Gottesfeld, S., 1991, “Polymer electrolyte fuel cell model”, *J. Electrochem. Soc.*, **138**(8), 2334-2342.
- [19] Barbir, F., 2005, *PEM Fuel Cells: Theory and Practice*, Academic Press.
- [20] Parthasarathy, A., Srinivasan, S. Appleby, A.J, 1992, “Temperature dependence of the electrode kinetics of oxygen reduction at the Platinum/Nafion interface – A microelectrode investigation,” *J. Electrochem. Soc.*, **139**(9), pp. 2530-2537.
- [21] Ge, S., Li, X., Yi, B., Hsing, I-M., 2005, “Absorption, desorption, and transport of water in polymer electrolyte membranes for fuel cells,” *J. Electrochem. Soc.*, **152**(6), A1149-A1157.
- [22] Eikerling, M., Kornyshev, A.A., Stimming, U., 1997, “Electrophysical properties of polymer electrolyte membranes: A random network model,” *J. Phys. Chem.*, **101**, pp. 10807-10820.
- [23] Jalani, N.H., Choi, P., Datta, R., 2004, “Phenomenological methanol sorption model for Nafion 117,” *Solid State Ionics*, **175**, pp. 815-817.
- [24] Lee, W-K., Ho, C-H., Van Zee, J.W., Murthy, M., 1999, “The effects of compression and gas diffusion layers on the performance of a PEM fuel cell,” *J. Power Sources*, **84**, pp. 45-51.
- [25] Wang, Y., Wang, C.-Y., 2005, “Transient analysis of polymer electrolyte fuel cells,” *Electrochimica Acta*, **50**, pp.1307-1315.